Unveiling the Interfacial Instability of the Phosphorus/Carbon Anode for Sodium-Ion Batteries

Wei Xiao,[†,‡] Qian Sun,[†] Mohammad Norouzi Banis,[†] Biqiong Wang,[†,‡] Jianneng Liang,[†] Andrew Lushington,[†] Ruying Li,[†] Xifei Li,[§] Tsun-Kong Sham,[*,‡] and Xueliang Sun[*,†]

[†]Department of Mechanical & Materials Engineering, University of Western Ontario, London, Ontario N6A 5B9, Canada

[‡]Department of Chemistry, University of Western Ontario, London, Ontario N6A 5B7, Canada

[§]Institute of Advanced Electrochemical Energy & School of Materials Science and Engineering, Xi'an University of Technology, Xi'an 710048, Shaanxi, China

Ⓢ *Supporting Information*

ABSTRACT: As a competitive anode material for sodium-ion batteries (SIBs), a commercially available red phosphorus, featured with a high theoretical capacity (2596 mA h g^{-1}) and a suitable operating voltage plateau (0.1−0.6 V), has been confronted with a severe structural instability and a rapid capacity degradation upon large volumetric change. In particular, the fundamental determining factors for phosphorus anode materials are yet poorly understood, and their interfacial stability against ambient air has not been explored and clarified. Herein, a high-performance phosphorus/carbon anode material has been fabricated simply through ball-milling the carbon black and red phosphorus, delivering a high reversible capacity of 1070 mA h g^{-1} at 400 mA g^{-1} after 200 cycles and a superior rate capability of 479 mA h g^{-1} at 3200 mA g^{-1}. More importantly, we first reveal the significance of inhibiting the exposure of phosphorus/carbon electrode materials to air, even for a short period, for achieving a good electrochemical performance, which would sharply decrease the reversible capacities. With the assistance of synchrotron-based X-ray techniques, the formation and accumulation of insulating phosphate compounds can be spectroscopically identified, leading to the decay of electrochemical performance. At the same time, these passivation layers on the surface of electrode were found to occur via a self-oxidation process in ambient air. To maintain the electrochemical advantages of phosphorus anodes, it is necessary to inhibit their contact with air through a rational coating or an optimal storage condition. Additionally, the employment of a fluoroethylene carbonate (FEC) additive facilitates the decomposition of the electrolyte and favors the formation of a robust solid electrolyte interphase layer, which may suppress the side reactions between the active Na−P compounds and the electrolyte. These findings could help improve the surface protection and interfacial stability of phosphorus anodes for high-performance SIBs.

KEYWORDS: sodium-ion batteries, phosphorus/carbon anode, interfacial instability, self-oxidation, FEC additive
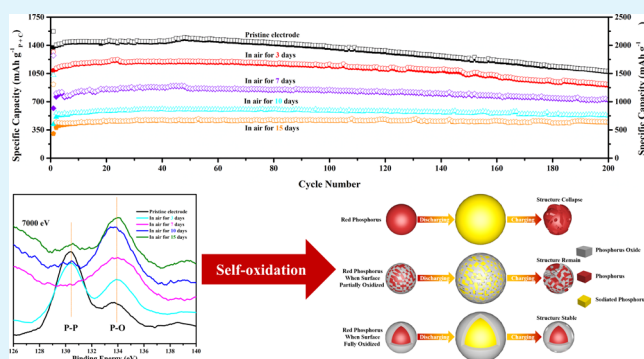
1. INTRODUCTION

The renaissance of sodium-ion batteries (SIBs) in the last decade has been parallel with the commercialization of lithium-ion batteries (LIBs), which have powered most portable electronics and futuristic electric vehicles. However, the rocketing price of lithium resources and their uneven distributions in remote areas, have gradually shifted the research focus on energy storage/conversion from LIBs to other affordable and sustainable candidates using alternative charging carriers.[1,2] Naturally, SIBs, accompanied with the ubiquitous sodium resources without toxicity and similar electrochemical reaction mechanisms originated from the sodium element located in the same group of the periodic table for lithium, have emerged as promising energy storage systems, particularly for the large-scale grid energy storage.[3−5]

Among all practical obstacles for the operative SIBs, the absence of an appropriate high-capacity anode used to determine their electrochemical feasibility and properties. The sodium (Na) metal anode generally suffers from a number of intrinsic safety challenges, including its low melting point (97.7 °C) and internal short circuits upon penetration of polymer separator by the grown dendrites during cycling.[6] Concurrently, carbon materials, such as graphite and disordered carbon materials, have very limited reversible capacities when used in SIBs compared to LIBs.[7−9] Based on the research experience for anode materials in LIBs, it is

promising to select a suitable alloy-type anode material for SIBs with a high theoretical specific capacity and a moderate redox potential, involving the multielectron reactions upon alloying and de-alloying.[7,8]

Phosphorus is an abundant element that can be easily extracted from the earth's crust and has been proposed as a candidate anode for the next-generation SIBs. Theoretically, one mol of phosphorus will react with three mols of sodium atoms to form Na_3P during the alloying process, yielding a high theoretical capacity of 2596 mA h g^{-1} within a desirable operating voltage range (0.1−0.6 V).[10] It is noteworthy that four different allotropes of phosphorus exist including white, violet, red (amorphous), and black phosphorus, with each presenting strikingly different physicochemical properties. For electrochemical use, white phosphorus is highly flammable and pyrophoric, whereas violet phosphorus can solely be prepared by heating red phosphorus for a long time. The complicated fabrication of black phosphorus involves an ultralong heating process under a high vacuum. Recently, the layer-structure phosphorene, exfoliated from black phosphorus, has been utilized as an anode material for LIBs[11,12] and SIBs.[13,14] Red phosphorus is thus left as a commercially available and inexpensive source.[15]

However, the structural collapse and subsequent electrode pulverization of red phosphorus because of the large volume expansion/shrinkage (∼292%) upon sodiation/desodiation would diminish the reversible capacity and cycle life for batteries. Furthermore, the low electronic/ionic conductivity of red phosphorus further weakens its rate capability.[16,17] In order to address the abovementioned challenges, several conductive materials, including flexible carbon materials (carbon black,[18,19] carbon nanotubes,[20] graphene,[13,21−23] 3D (three-dimensional) carbon,[24] carbon composite[14]), electrochemically active material/carbon materials (Sn_4P_3,[25] SnP_3,[26] Se_4P_4,[27] and GeP_5[28]), and electrochemically inactive metal/carbon materials (FeP,[29] CuP_2,[30] Ni_2P,[31] and $P-TiP_2-C$[32]), have been employed to buffer the large volume variation and improve the electronic/ionic conductivity as well as electrochemical reversibility/durability of red phosphorus. Additionally, the phosphorus particles have been introduced by an evaporation−condensation method into several conductive and robust structures, including porous carbon,[33] carbon nanofibers,[34] carbon nanotubes,[35,36] mesoporous carbon,[37] metal−organic framework-derived microporous carbon,[38] graphene paper,[39] and aerogel.[40] Very recently, the successful liquid syntheses of iodine-doped phosphorus nanoparticles[41] and hollow red phosphorus nanospheres[42] have further demonstrated the strong capability of nanotechnology in this emerging field. Among these approaches, loading phosphorus into the carbon host is considered as a universal and effective route.

As the electronic structure of phosphorus is $3s^2 3p^3$, it should be easily oxidized and generally exists as inorganic phosphate. Even though black phosphorus is the most thermodynamically stable among the available crystal phases, it rapidly reacts with O_2/H_2O in ambient air, which degrades its electrical properties.[12,43] However, the understanding on the stability of red phosphorus (or phosphorus-based composites) in ambient air, and especially the effects of such interfacial instability on its electrochemical performance for SIBs, is yet lacking. At the same time, the impact of the structural change in ambient air on the corresponding electrochemical performance is also unknown. Therefore, it is appealing to gain a more

thorough understanding of air stability for red phosphorus-based electrodes.

In this regard, we have synthesized phosphorus/carbon composites through a conventional ball-milling method, identified the effects of air exposure time for phosphorus electrodes on their electrochemical properties, and studied the chemical evolution of passivation surface in these conditions, which can provide strategic insights into interfacial stability and surface protection toward the development and application of phosphorus-based electrodes.

2. EXPERIMENTAL SECTION

2.1. Materials' Synthesis. Phosphorus/carbon composites were prepared by planetary ball-milling at 600 rpm for 24 h to mix the commercial red phosphorus (purity > 97%, Sigma-Aldrich) with porous carbon (Ketjen black, EC600JD). On the basis of the previous reports, the weight ratio of red phosphorus to porous carbon was 7:3.[18,19] The weight ratio of stainless-steel ball-milling balls to all starting materials was 20:1. In order to fully pulverize the large particles of red phosphorus and produce a homogeneous mixture, three balls with different diameters (3, 5, 8 mm) were employed in a weight ratio of 1:1:1, respectively. After initially weighing the starting materials and different stainless-steel balls, all parts were mixed in a steel vial and sealed in a glove box filled with argon.

2.2. Electrochemical Measurement. Initially, the conductive agent (acetylene black), Na-CMC (sodium carboxymethyl cellulose, low viscosity, EMD Millipore) binder, and active material (phosphorus/carbon composite) were dissolved into an appropriate amount of distilled water using a weight ratio of 1.5:1.5:7, respectively. Additionally, carbon black, acetylene black, and [poly-(vinylidene difluoride)] binder with a mass ratio of 8:1:1 were first mixed and then dissolved into (N-methyl-2-pyrrolidone), respectively. The as-prepared homogeneous slurry was then cast onto a clean copper foil and further dried at 60 °C under vacuum overnight. Electrodes were punched into to 1/2 inch pellets and subsequently pressed, yielding a loading mass of ∼1.5 mg cm^{-2} per pellet. To study the air (in)stability of phosphorus/carbon electrodes and their effects on their electrochemical performances, four pellets were selected and placed in ambient environment for 3, 7, 10, and 15 days, respectively.

Half-cell configuration 2032-type coin cells, employing a phosphorus/carbon electrode as a cathode, a polypropylene membrane (Celgard 3501) as a separator, and sodium metal as an anode immersed in electrolyte, were assembled in an Ar-filled glove box. The electrolyte was prepared by dissolving 1.0 mol L^{-1} sodium perchlorate ($NaClO_4$) into a solution of ethylene carbonate (EC) and diethyl carbonate electrolyte by 1:1 in volume with addition of 10 wt % fluoroethylene carbonate (FEC). The electrochemical behavior of phosphorus electrodes was evaluated using cyclic voltammetry (CV) in a Biologic VMP3 electrochemical station at a sweep rate of 2 mV s^{-1}. Galvanostatic charge/discharge performance was evaluated between 0.001 and 2.0 V (vs Na/Na^+) at various current densities under room temperature using a LAND (Wuhan Kingnuo Electronics, China) cycler.

2.3. Physical Characterization. The crystalline structures of ball-milled compounds were identified using X-ray diffraction (XRD) with a Bruker D8 ADVANCE (Cu Kα source, 40 kV, 40 mA) spectrometer. Raman spectroscopy measurements were conducted using a HORIBA Scientific LabRAM HR spectrometer system equipped with a 532.4 nm laser. The morphologies of the initial materials and phosphorus/carbon composite were observed using a Hitachi S-4800 field emission scanning electron microscope operated at 5 keV and a high-resolution transmission electron microscopy (TEM) (JEOL 2010 FEG) equipped with an energy-dispersive X-ray spectrometer. For the synchrotron-based X-ray characterizations, the P K-edge X-ray absorption spectroscopy (XAS) in fluorescence yield mode and P L-edge XAS in total electron yield mode were measured under high vacuum in Soft X-ray Microcharacterization Beamline (SXRMB) and Variable Line Spacing Plane Grating Monochromator
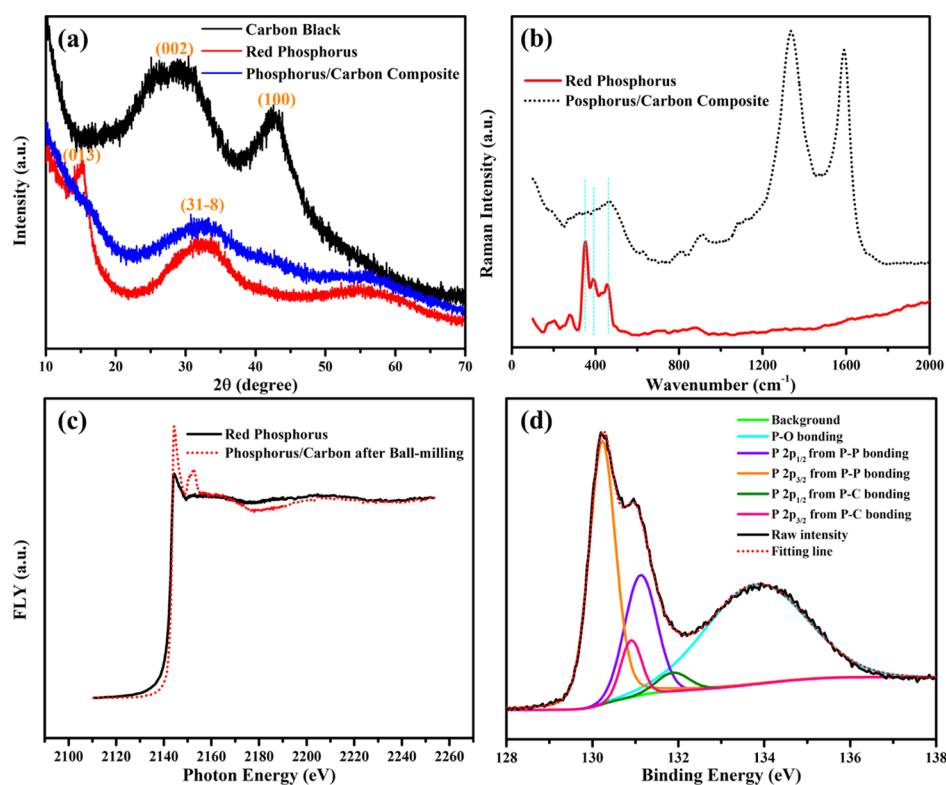
Figure 1. (a) XRD patterns for carbon black, red phosphorus, and phosphorus/carbon composite. (b) Raman spectra and (c) P K-edge X-ray absorption spectroscopies for red phosphorus and phosphorus/carbon composite. (d) Synchrotron-based surface-oriented P 2p XPS for phosphorus/carbon composite.

(VLS-PGM) in Canadian Light Source (CLS), respectively. The surface-oriented high-resolution X-ray photoelectron spectroscopy (XPS) was collected at the VLS-PGM beamline with a pass energy of 20 eV and an excitation energy of 230 eV. The depth-oriented high-resolution XPS was recorded at the SXRMB beamline with a pass energy of 200 eV using three different excitation energies of 3000, 4900, and 7000 eV, respectively.

3. RESULTS AND DISCUSSION

3.1. Characterization of Phosphorus/Carbon Electrode Materials. XRD was employed to evaluate the crystal structures of starting materials and the phosphorus/carbon composite. In Figure 1a, the XRD of carbon black shows two broad peaks around 26° and 43°, which can be indexed to the (002) phase mode of graphite and the (100) phase mode of the ordered hexagonal structure in graphite.[9,44] The XRD of commercial red phosphorus displays three obvious peaks, including a sharp peak at 15° for the (013) diffraction plane, a strong broad peak at 32° for (31−8) diffraction plane, and a weak broad peak at 55°, hinting at a medium-range ordered structure in monoclinic phosphorus (JCPDS no. 00-044-0906, space group of $P2/c$).[35,38,45] Interestingly, two broad peaks at 32° and 55° can be observed for the phosphorus/carbon composite, demonstrating the phase preservation of amorphous red phosphorus after the ball-milling process. Owing to the severe destruction of medium-range ordered structure upon high-energy ball-milling, the obvious (013) peak at 15° in pristine red phosphorus completely disappears in the XRD pattern for the phosphorus/carbon composite, whereas the vanishment of (002) and (100) features for carbon black in the phosphorus/carbon composite further indicates the uniform dispersion of totally crushed red phosphorus clusters in carbon

matrixes, which are in good agreement with the previous results for phase transformation and structural evolution of ball-milled phosphorus/carbon composites.[18,19,21,45,46]

Similar to the Raman spectroscopy of carbon black in Figures S1, Figure 1b also shows two strong peaks at 1334 and 1590 cm^{-1} for the phosphorus/carbon composite, which can be attributed to the D band of a disordered sp^3 carbon phase and G band of a graphitic sp^2 carbon structure in amorphous carbon black, respectively.[9,14] Normally, the P7 and P9 cages in amorphous red phosphorus are utilized to construct pentagonal tubes in coupled layers, whereas the sharp peak around 350 cm^{-1} is originated from P9 cages.[47] Hence, the existence of the phosphorus element in the composite can be verified by three peaks of P−P bonding between 300 and 500 cm^{-1} for red phosphorous and phosphorus/carbon composite. Additionally, the relatively lower intensities for these peaks may have resulted from the partial breakup of P−P bonding and generation of P−C bonding upon the formation of phosphorus/carbon composite, whereas the amorphous carbon would also cover the surface of red phosphorus, further weakening the signal strength.[18,19,21]

Basically, the emergence of X-ray absorption at the P K-edge should be due to the electron transition from the 1s core level to the 3p unoccupied orbital.[48] Comparing the P K-edge X-ray absorption spectroscopies of red phosphorus and the phosphorus/carbon composite, a stronger peak around 2144.5 eV is found for the composite as shown in Figure 1c. This not only agrees with the K-edge in the P4 molecule, but also implies a decrease in the size of red phosphorus with a high feedback intensity.[48] Concurrently, a new peak as observed at 2152.5 eV should be ascribed to the partial oxidation of phosphorus,[49−51] corresponding well with the
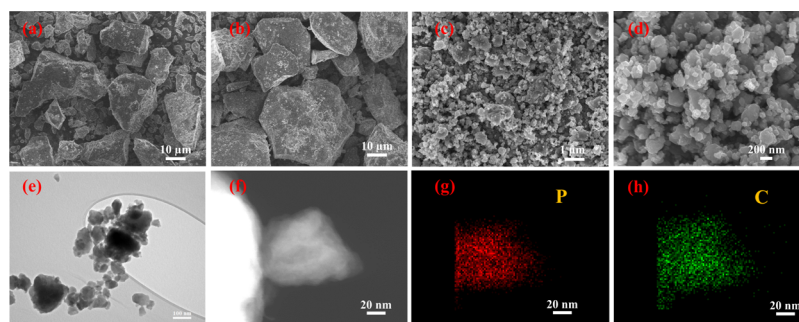
Figure 2. SEM images of (a,b) red phosphorus and (c,d) phosphorus/carbon composite. (e) Low-magnification TEM image, (f) high-magnification TEM frame and the corresponding (g) P, (h) C elemental mappings for phosphorus/carbon composite.
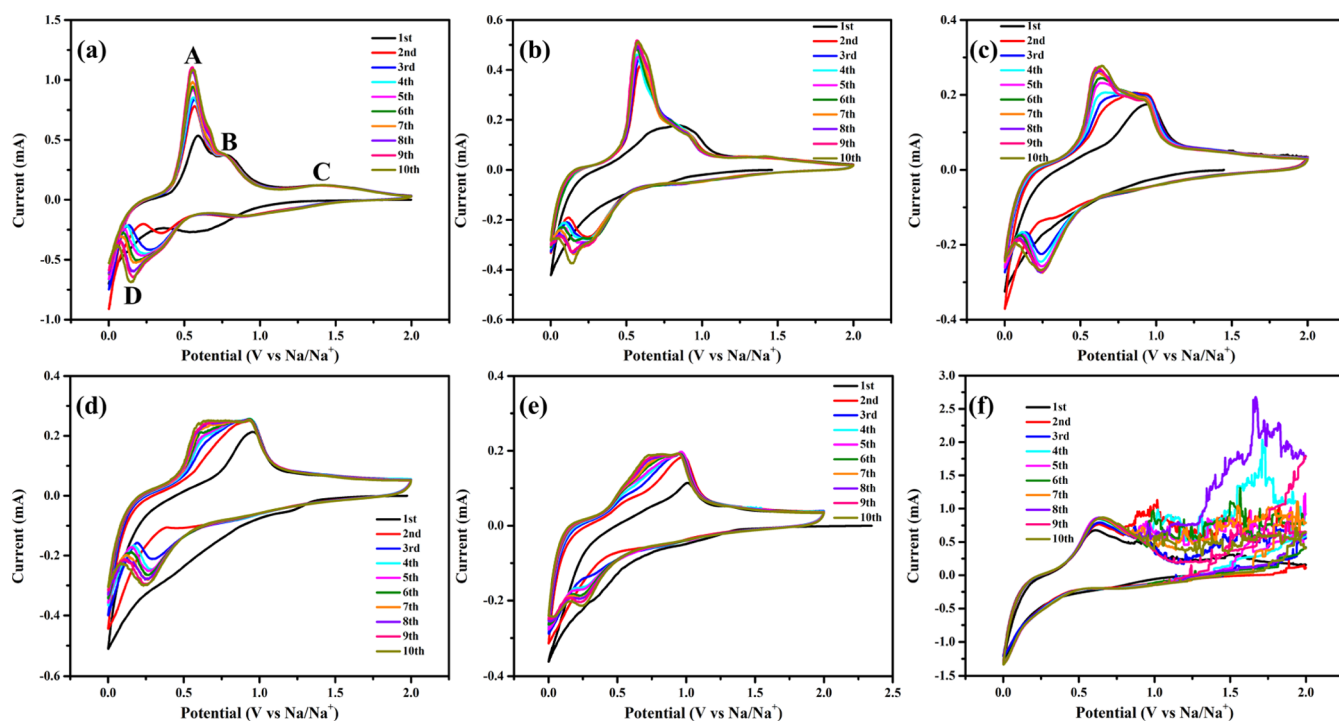

Figure 3. CV curves of (a) the pristine electrode, the electrode exposed in air for (b) 3 days, (c) 7 days, (d) 10 days, and (e) 15 days with FEC additive in the electrolyte, and (f) the pristine electrode without FEC additive in the electrolyte at a scan rate of 0.2 mV s^{-1}.

XPS data obtained for the phosphorus/carbon composite, as shown in Figure 1d. According to the previous reports on the peak-fitting for XPS,[21,24,39] these two broad peaks can be deconvoluted into five individual peaks. The sharp peaks at 132.2 and 131.2 eV are related to the P $2p_{3/2}$ and P $2p_{1/2}$ characteristics from the P−P bonding, whereas the two weaker peaks at 131.9 and 130.9 eV are derived from the P $2p_{3/2}$ and P $2p_{1/2}$ features for the P−C bonding, respectively. Moreover, a broad peak at 133.8 eV is originated from the strong P−O bonding, which had also been found in various phosphorus anode materials obtained from the ball-milling approach,[21,22,32,46] evaporation−condensation method,[52] and chemical routes.[11,41,42] On the basis of the previous physical characterizations, it is clear that the phosphorus/carbon composite has primarily maintained most of the red phosphorus features and inevitably suffered from the phosphorus oxidation.

The morphologies of red phosphorus and phosphorus/carbon composite were compared in Figure 2a−d alongside the elemental distributions of P and C in Figure 2e−h. As depicted in Figure 2a,b, the large red phosphorus particles with

the sizes ranging from 10 to 50 μm are loosely stacked and unevenly distributed. From the SEM pictures, the diameters of the most phosphorus/carbon particles are found to be below 400 nm, as shown in Figure 2c,d. Additionally, several microparticles are irregularly distributed among the nanoparticles. Regardless of the partial aggregation for tiny granules with the size below 100 nm in Figure 2e, the phosphorus/carbon composite in Figure 2f−h realized the elemental enrichments of P and C, proving a homogeneous integration of phosphorus with carbon.

3.2. Electrochemical Measurement of Phosphorus/Carbon Electrode Materials. CV was performed at a scan rate of 0.2 mV s^{-1} between 0.001 and 2.0 V (vs Na$^+$/Na) to understand the effects of air-aging for phosphorus electrodes on their electrochemical behaviors, as presented in Figure 3. During the initial sodiation process of the pristine electrode, a single irreversible broad peak can be found at 0.61 V, corresponding to the decomposition of the electrolyte and generation of a solid electrolyte interphase (SEI) layer. Additionally, a series of anodic features at 0.55, 0.79, and 1.42 V represent a stepwise phase conversion of Na$_3$P to Na$_2$P,
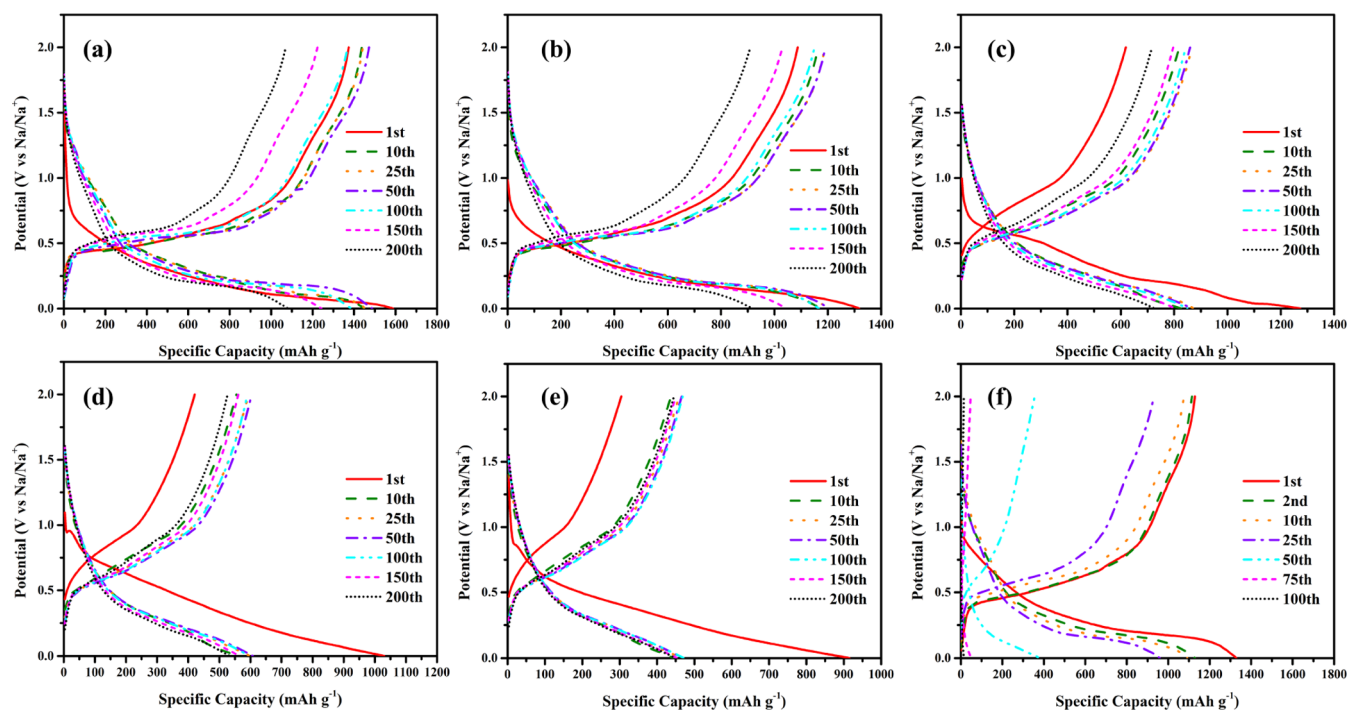
Figure 4. Discharging and charging profiles of (a) the pristine electrode and the electrode (b) in air for 3 days, (c) 7 days, (d) 10 days, (e) 15 days with the FEC additive in the electrolyte, and (f) the pristine electrode without the FEC additive in the electrolyte at a current density of 400 mA g^{-1}.

NaP, and NaP$_7$ intermediates, respectively.[18,37,46] Importantly, the peak in the D region reflects the sodiation process, whereas the peaks in the A, B, and C regions orderly correspond to the desodiation process. In the subsequent cycles, the cathodic peaks gradually move to the D region of 0.35−0.14 V, whereas the anodic features remain in the same positions of the A, B, and C regions. When comparing electrodes exposed to air for 3, 7, 10, and 15 days, the first irreversible cathodic peak and subsequent anodic peak in the C region almost disappear. Even though the anodic peaks for the D region in the repeated cycles are located around 0.24 V, the cathodic peaks within the A and B regions gradually move from 0.55/0.79 V to the higher voltages of 0.57/0.91, 0.62/0.93, 0.62/0.94, and 0.72/0.96 V with the increase of air exposure time, respectively, suggesting an increased electrochemical polarization because of the emergence and evolution of the surface passivation layer. Concurrently, the peak intensity within the A region rapidly decreases, whereas the B region peaks gradually increase in intensity. An increase in the voltage polarization, as identified in Figure 3a−e, can be attributed to the gradual oxidation of the phosphorus electrodes, which not only reduces the amount of active materials, but also impedes the electronic/ionic migrations by accumulating the insulating phosphorus/oxygen compounds. Moreover, the vital role of the FEC additive in the electrolyte for phosphorus anode has also been revealed in Figures 3f and S8. Specifically, no irreversible peak can be found around 0.61 V in the first discharging process, implying the absence of a robust and stable SEI layer during the initial sodiation process. Without the formation of an electronically insulating and ionically conductive SEI layer, the highly active sodium/phosphorus alloy compounds would continuously react with the electrolyte, leading to electrochemical failure during the discharging/charging processes. It is obvious to find that severe parasitic reactions between sodium/phosphorus

alloy compounds and electrolyte are prone to happen at the charging process, resulting in the irregular CV curves upon the desodiation process.

The electrochemical performances of the pristine electrode and electrodes in air for different days were evaluated by the galvanostactic discharge−charge tests, as shown in Figure 4. The pristine electrode delivers an initial discharging capacity of 1572 mA h g^{-1} and a highly reversible charging capacity of 1373 mA h g^{-1}. As the reversible capacity of carbon black is as low as 107.4 mA h g^{-1} in the first cycle, its contribution to the reversible capacity of the phosphorus/carbon composite can be negligible. Interestingly, the electrodes exposed to air for 3, 7, 10, and 15 days demonstrate the decreased charging capacities of 1087, 618, 420, and 304 mA h g^{-1}, respectively. Furthermore, the first coulombic efficiency is also found to decrease from 89.3% for the pristine electrode to 82.5, 48.5, 40.8, and 33.2% for the electrodes in air for 3, 7, 10, and 15 days, respectively. The rapidly decreasing specific capacity and coulombic efficiency correlated well with the air exposure time, clearly demonstrating the electrochemical deterioration of phosphorus electrodes because of the self-oxidation process. Moreover, the gradual increase of charging voltage plateau in Figure 4 agrees well with the position change found for the anodic peaks in Figure 3. This obvious voltage hysteresis further decreases the electrochemical stability of phosphorus electrodes in air. Additionally, the increase of the specific capacity during the electrochemical activation of phosphorus electrodes at the beginning of cycling process also increases along with the air exposure time because of the accumulation of phosphorus/oxygen compounds in phosphorus/carbon composites.

Among all the samples tested, the fresh pristine electrode could display the large discharging capacities of 1450, 1454, 1487, 1387, 1243, 1080 mA h g^{-1} and highly reversible
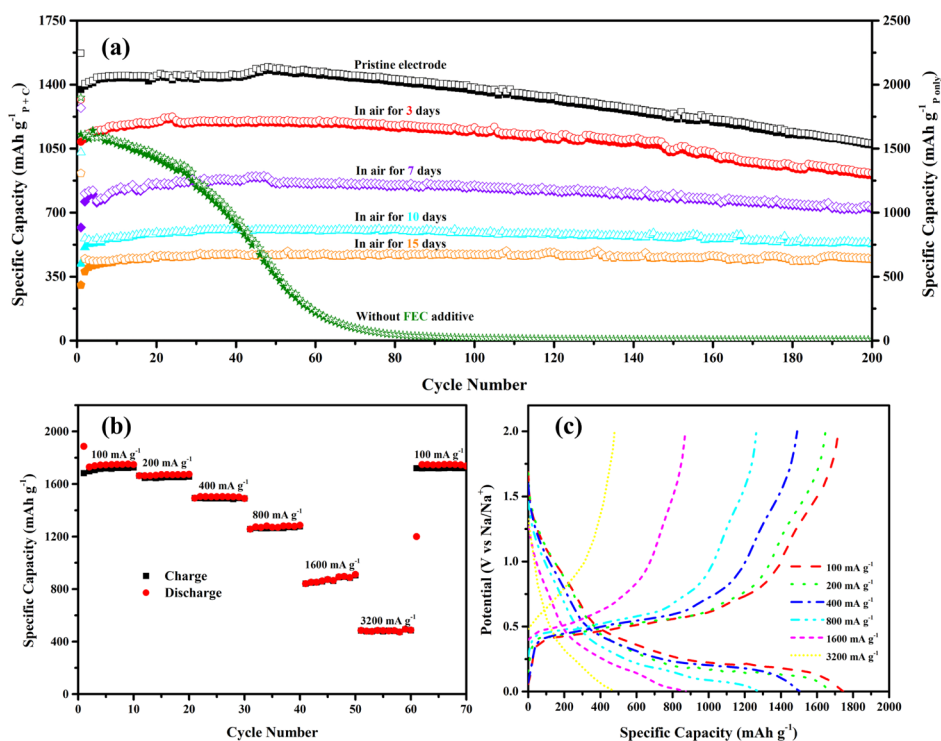
Figure 5. (a) Cycle performances of the pristine electrode, the electrodes exposed to air for different days with the FEC additive in the electrolyte, and the pristine electrode without the FEC additive in the electrolyte at a current density of 400 mA g^{-1}. (b) Rate performance and (c) the corresponding discharging and charging profiles for the pristine electrode at different current densities.

charging capacities of 1437, 1442, 1472, 1369, 1223, 1070 mA h g^{-1} at the 10th, 25th, 50th, 100th, 150th, 200th cycles, respectively. These electrochemical results are comparable to those reported values in the literature with similar phosphorus/carbon systems.[14,18−21,23,24,32,35,36,40,46] For the pristine electrode studied without the use of the FEC additive, the initial discharging and charging capacities of 1329 and 1128 mA h g^{-1} were determined, respectively. However, the charging voltage plateau rapidly increases in the following cycles, whereas the discharging voltage plateau remarkably decreases, leading to the fast capacity diminishment and ultimate electrochemical failure. As the FEC additive in the electrolyte would facilitate the emergence of a robust, stable, and flexible SEI layer on the surface of high-capacity alloy-type anodes to maintain the structural integrity upon huge volume change and suppress the side reactions of the unstable electrode with reactive electrolyte, the pristine phosphorus/carbon electrode in the electrolyte without the FEC additive would continuously aggravate the electrolyte decomposition on the newly formed interfaces upon repeated huge volume change, and suffer from the gradual collapse of the structure, severe pulverization of the electrode, eventual depletion of the electrolyte, and rapid degradation of the capacity.[53,54]

Figure 5a presents the systematic investigation of cycle performances for the electrodes exposed to air for different lengths of time. Clearly, the initial capacity decreases for electrodes left in air for a longer period. Compared with a first charging capacity of 1373 mA h g^{-1}, the pristine electrode demonstrates a highly reversible capacity of 1070 mA h g^{-1}, corresponding to 1528 mA h g^{-1} as 58.9% of the theoretical specific capacity for P (2596 mA h g^{-1} corresponding to the formation of Na$_3$P), after 200 cycles at 400 mA h g^{-1}. For electrodes left under ambient conditions for 3, 7, 10, and 15

days, the charging capacities of 902, 716, 526, and 445 mA h g^{-1} are observed for over 200 cycles, respectively. Furthermore, a fast capacity degradation disables the electrochemical capability of the pristine electrode without utilizing the FEC additive in the electrolyte (Figure S9). However, a comparison of the cycling stability for different electrodes further poses a question regarding the phase evolution of phosphorus electrodes in air. Compared with the decreased capacities for electrodes in air for more days, the capacity retention initiated from the 20th to 200th cycle after the electrochemical activation increases from 74.3% for the pristine electrode to 75.8, 83.7, 89.6, and 98.4% for the electrodes in air for 3, 7, 10, and 15 days, respectively. This phenomenon on the improved electrochemical cycle stability is an emergent property dependent on two factors. On the one hand, a decreased amount of active materials coupled with a self-oxidation process may lead to a lower specific capacity, imposing the weaker evolutions of volume expansion/shrinkage on electrode structures. On the other hand, a gradual accumulation of phosphorus/oxygen compounds on the surface may help to buffer the low-level volume changes for phosphorus/carbon electrodes upon cycling. As displayed in Figure 5b,c, the pristine electrodes deliver the reversible capacities of 1719, 1647, 1490, 1264, and 871 mA h g^{-1} at the current densities of 100, 200, 400, 800, and 1600 mA g^{-1}, respectively. When cycled at 3200 mA g^{-1}, the pristine electrode could still present a highly reversible capacity of 479 mA h g^{-1}. After 65 cycles at high current densities, the charging capacity could return to 1719 mA h g^{-1}. In terms of the strikingly different electrochemical properties for electrodes in different conditions, it is quite urgent to explore their structural evolution and phase transformation in ambient air.
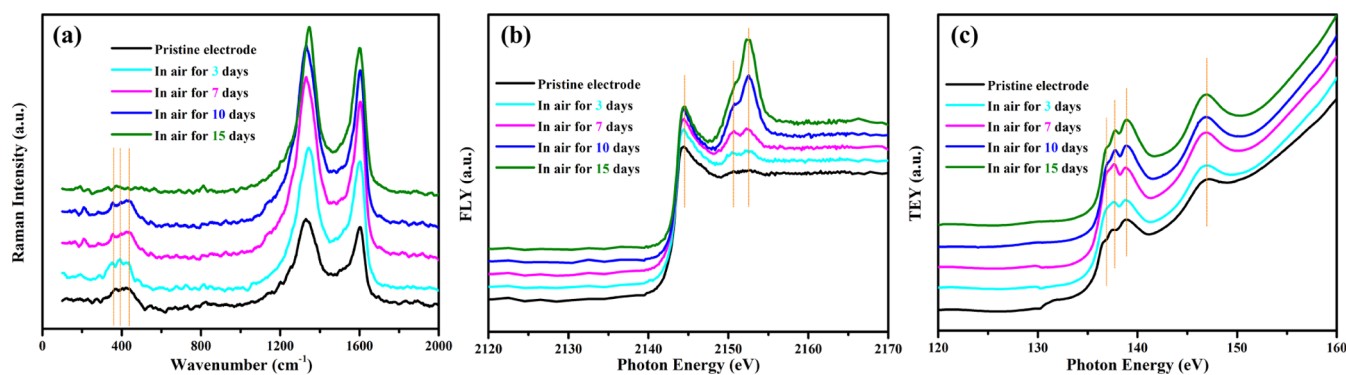
Figure 6. (a) Raman spectra, (b) P K-edge, and (c) P L-edge X-ray absorption spectroscopies for the pristine electrode and electrodes in air for different days.
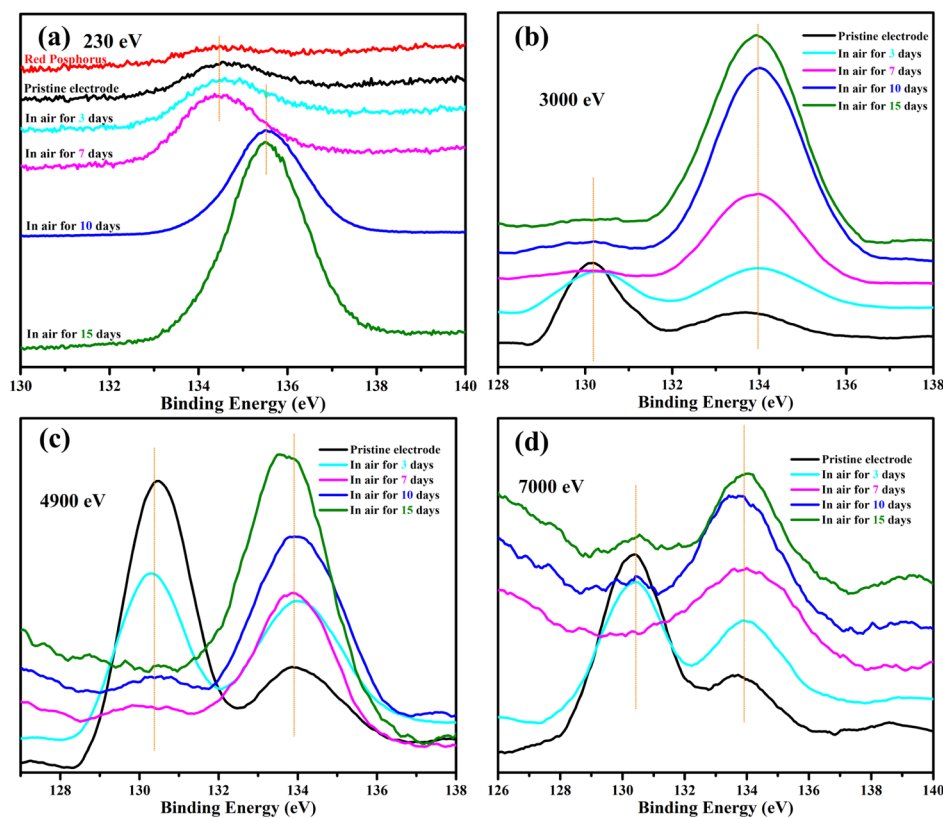

Figure 7. (a) Surface-oriented and (b−d) depth-oriented P 2p X-ray photoemission spectroscopies with different photon energies for the red phosphorus, the pristine electrode, and the electrodes in air for different days.

3.3. Self-Oxidation Mechanism for Phosphorus/Carbon Electrode Materials.

As shown in Figure 6a, the Raman spectra display three features in the range of 300−500 cm^{-1}, indicating the existence of phosphorus in the aged electrodes. However, the decreasing intensity of these peaks with the increasing air exposure time further provides the evidence for the gradual growth of phosphorus/oxygen compounds on the electrode surface. P K-edge X-ray absorption spectroscopies presented in Figure 6b were employed to understand the structural evolution of phosphorus electrodes in air. The strong peak at 2144.5 eV is related to 1s core-level electron transitions to the vacant t2*(p-like) antibonding orbitals, whereas another two peaks at 2150.6 and 2152.5 eV arise from the shape resonance or the multiple scattering.[55,56] In this circumstance, the major K-edge at a lower energy position reflects the P−P bonding, whereas

another two peaks at the high energy region may have resulted from the P−O bonding in the species of $(PO_2)^{3-}$ and $(PO_4)^{3-}$, respectively.[12,57−59] The decrease of the peak intensity for the P−P bonding (2144.5 eV) and increase of peak intensity for the P−O bonding (2152 eV) with the increasing duration in air further confirm the accumulation of phosphate compounds and loss of active phosphorus. X-ray absorption spectroscopies performed at the P L-edge presented in Figure 6c display two peaks at 136.9 and 137.7 eV as a result of the electron transitions from the $2p_{3/2}$ and $2p_{1/2}$ levels after the spin−orbit split 2p into the first unoccupied 3s-like antibonding state, respectively.[56,60,61] A peak at 138.9 eV resulted from the mixed-valence band electron transitions.[62] However, several other publications suggest that this signal originates from the electron transitions to a 3p-like antibonding state, considering the possible mixture of this signal with other features from

oxygen and metals.[61,63,64] A broad peak at 147.0 eV stems from the 2p to 3d transitions.[61] For the pristine electrode, the positions of peaks for the electron transitions from split 2p orbitals to 3s-like antibonding state are shifted to the higher energy regions. The increasing intensity ratios of the peak at 137.7 eV to the peak at 136.9 eV for electrodes aged in air also verify the structural distortion of phosphate tetrahedron, which conforms to the continuous growth of phosphate compounds on the surface of phosphorus particles.

The surface and depth-oriented X-ray photoemission spectroscopies were employed to understand the phase evolution of phosphorus electrodes in air, providing a unique benefit of allowing for a variable analyzing depth by adjusting the excitation photon energy. Utilizing a low photon energy of 230 eV, only one peak at 134.5 eV, corresponding to the P–O bonding from $(PO_4)^{3-}$ or $(PO_2)^{3-}$ compounds, is observed in Figure 7a for the red phosphorus, the pristine electrode, and the electrodes exposed to air for 3 and 7 days.[11,12,42,46,57−59] After exposing the electrodes to ambient conditions for 10 and 15 days, the P−O bonding peak is shifted to 135.5 eV, indicating the structural distortion of phosphate after the continuous reactions between phosphorus and oxygen. Increasing the excitation photon energy to 3000 eV, allowing for a deeper penetration level, the peak for the P 2p feature can be found at 130.2 eV for the pristine electrode, whereas the peak intensities of P−O bonding at 134.0 eV for electrodes under different conditions increase along with the air-aging periods, as shown in Figure 7b. In Figure 7c,d, the peak intensities for the lower-energy P−P bonding decrease and the peak intensities for the high-energy P−O bonding increase with the longer air exposure time. Namely, the thickness of phosphate layers increases with the exposure to ambient air.

To further understand the effects of water and oxygen on the self-oxidation process for phosphorus, P L-edge X-ray absorption spectroscopies were further conducted to explore the structural evolution and phase transformation of the pristine phosphorus/carbon composite in water and oxygen after 24 h. In Figure 8, an obvious peak at 131.6 eV, which represents a strong P−P bonding in the pristine phosphorus/carbon composite, would remarkably decrease its intensity after aging in water and finally disappear upon contacting oxygen for 24 h, indicating the partial degradation in water and
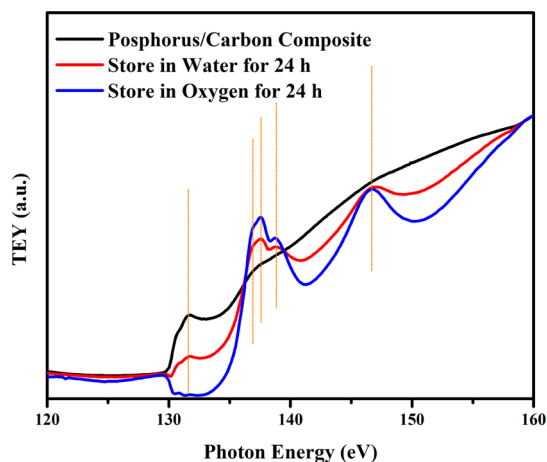
severe oxidation in oxygen for active phosphorus. At the same time, four new peaks at 136.9, 137.5, 138.8, and 147.0 eV emerge in the samples aged in water and oxygen, further indicating the oxidation of phosphorus in different conditions. Specifically, the noticeable two peaks at 136.9 and 137.5 eV should be attributed to the electron transitions from the split spin orbitals at $2p_{2/3}$ and $2p_{1/3}$ states to the first unoccupied 3s-like antibonding level, respectively. Additionally, a weak peak at 138.8 eV can be either assigned for the electron transitions to a mixed valence band or a 3p-like antibonding state. Furthermore, a broad peak at 147.0 eV resulted from the 2p to 3d electron transitions in d-like shape resonances for amorphous and crystalline phosphate.[55,56,60,61] Even though the gradual oxidation and severe degradation of phosphorus can be identified in water and oxygen, it is still challenging to distinguish the fundamental roles of water and oxygen in the self-oxidation process for the phosphorus/carbon composite. Particularly, oxygen rather than water was found to primarily induce the decomposition of thermodynamically stable black phosphorus, which may throw light on the self-oxidation mechanism of the phosphorus/carbon anode in ambient air.[65]

On the basis of the spectroscopic insights into the chemical evolution of phosphorus electrodes, and their electrochemical relationship of a better cycle stability with a longer air exposure time, the schematic diagram for the fresh and oxidized red phosphorus is presented in Figure 9 For the pristine electrode, the fresh red phosphorus particles have a large contact area with the conductive agent and mixed carbon black, contributing to a large reversible capacity and a superior rate capability in the facile formation and decomposition of Na_3P. However, the alloying/dealloying processes for this pristine material with 3 Na per atom inevitably result in the large volume expansion/shrinkage (up to a changing rate of 300%), inducing a structural collapse, an electrode pulverization, and subsequently a fast capacity degradation. When the surface of red phosphorus is partially oxidized, as with the case for the electrodes left in air for 3 and 7 days, the mass of active phosphorus material slightly decreases, leading to the less drastic volume changes during the sodiation/desodiation processes. Although the as-formed passivation layers in a self-oxidation process can partially accommodate the poorer volume variations, the few red phosphorus particles would still crack after the repeated cycles and lose the electric contact with the copper foil, giving rise to the decrease of the reversible capacity upon cycling. When the surface of red phosphorus particles is fully oxidized for electrodes aged in air for 10 and 15 days, there is a drastic decrease in active material with the minimal volume changes, leading to a highly reversible capacity and a stable cycle performance. However, this structural robustness imparted by the insulating phosphate comes with an impact on specific capacity and energy density. Consequently, the full utilization of phosphorus and its composites for battery applications is highly dependent on a self-oxidation process. Namely, it is imperative to inhibit the physical contact between phosphorus electrodes and ambient air through optimizing the storage conditions and conduct the interfacial modifications for the phosphorus/carbon electrode without sacrificing their electrochemical performance. Atomic layer deposition (ALD) and molecular layer deposition (MLD), as ideal coating techniques with the nanoscale thickness, deposition uniformity, and conformity, could be the powerful routes to engineer the passive coating layers for inhibiting this self-oxidation behavior.[66−70] Particularly, the rational con-

Figure 8. P L-edge X-ray absorption spectroscopies for the pristine phosphorus/carbon composite and phosphorus/carbon composite stored in water and oxygen for 24 h.
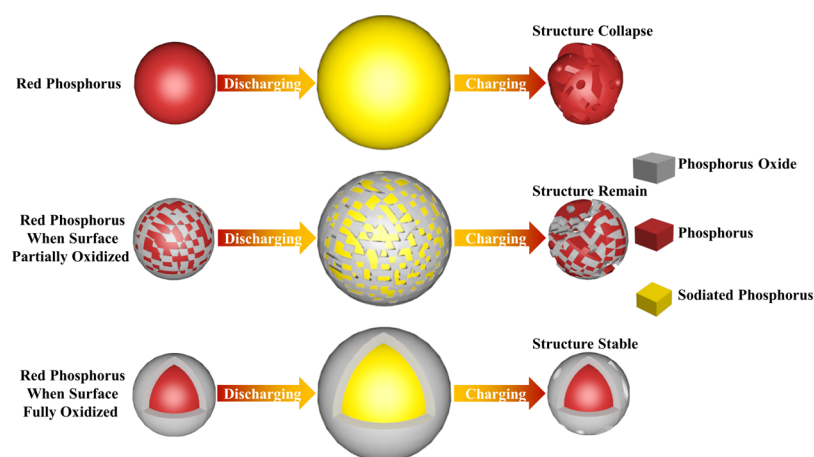
Figure 9. Schematic diagram of structural evolutions during the sodiation/desodiation processes for the fresh and oxidized red phosphorus.

struction of robust, flexible, and stable composite coating layers through the combinations of ALD and MLD would not only maintain the structural integrity of the phosphorus anode upon a huge volume expansion/shrinkage, but also suppress the severe interfacial reactions of the phosphorus anode against ambient air and reactive electrolyte. Different from the fresh phosphorus anode chronically suffering from the huge volume change and rapid capacity degradation, the mildly oxidized phosphorus anode, presenting a significantly improved cycling stability with a relatively capacity loss, can be a promising base material for rational surface coating.

4. CONCLUSIONS

In summary, a phosphorus/carbon composite was fabricated using a conventional ball-milling technique. When applied as an anode material for SIBs, the pristine electrode delivered an initial discharge capacity of 1572 mA h g^{-1} with a coulombic efficiency of 89.3%. Furthermore, a reversible capacity of 1070 mA h g^{-1} was obtained over 200 cycles at 400 mA g^{-1}. These promising results may be attributed to the elimination of self-oxidation for the phosphorus/carbon electrode in ambient air. The electrodes exposed to the ambient air displayed significantly decayed electrochemical properties, compared to the pristine electrode. On the basis of the Raman and synchrotron-based X-ray absorption/photoelectron spectroscopies, we observed the gradual formation and evolution of surface phosphate layers via a self-oxidation process. Although these phosphate layers may somehow contribute to stabilizing the phosphorus particle from the large detrimental volume changes, the loss of active materials and accumulation of insulating layers would deteriorate the electrochemical reversibility and stability for phosphorus/carbon electrodes. In addition, the function of a robust SEI layer, that resulted from the decomposition of the electrolyte with the assistance of FEC additive in the electrolyte, has been electrochemically confirmed in suppressing the side reactions between active electrode surface and electrolyte. The novel discovery on the relationship between electrochemical activity/stability and phase evolution on the phosphorus surface could throw light on storing conditions and interfacial designs of phosphorus-based anode materials for high-performance SIBs.

■ ASSOCIATED CONTENT

Ⓢ Supporting Information

The Supporting Information is available free of charge on the ACS Publications website at DOI: 10.1021/acsami.9b07884.

Raman spectroscopy of carbon black; SEM images of phosphorus/carbon composite at magnifications of (a) 20 000 and (b) 10 000 times; XRD patterns of the pristine electrode and the electrodes in air for different days; cycle performances of the pristine electrode at 100 and 200 mA g^{-1}; cycle performances of the pristine electrode at 400 and 800 mA g^{-1}; cycle performances of the pristine electrode at 1600 and 3200 mA g^{-1}; comparison of the cycle performances for the pristine electrode with those in other reports; CV curves of pristine phosphorus/carbon electrode in electrolyte without addition of FEC at a scan rate of 0.2 mV s^{-1}; cycle performances of pristine P/C electrodes in electrolytes with and without the FEC additive; cycle performance of carbon black in the electrolyte with the FEC additive; discharge and charging curves of carbon black in the electrolyte with the FEC additive; comparison of cycling parameters (PDF)

■ AUTHOR INFORMATION

Corresponding Authors
*E-mail: tsham@uwo.ca (T.-K.S.).
*E-mail: xsun9@uwo.ca (X.S.).
ORCID Ⓘ
Mohammad Norouzi Banis: 0000-0002-6144-6837
Biqiong Wang: 0000-0002-3903-8634
Xueliang Sun: 0000-0003-2881-8237

Author Contributions

W.X. conceived the idea, designed the experiment, conducted the data analysis, and wrote the paper under the guidance of X.S. and T.-K.S.. Q.S. helped to organize the writing structure and made the revisions. M.N.B. and B.W. collected the synchrotron data from CLS. A.L. helped to polish the language of the paper. X.L. provided the suggestions for the experiment results and paper writing. R.L. and J.L. carried out the general characterizations in the laboratory. All the authors discussed the experimental results and proof-read the final paper.

Notes

The authors declare no competing financial interest.

■ REFERENCES

(1) Tarascon, J.-M. Is Lithium the New Gold? *Nat. Chem.* **2010**, *2*, 510.

(2) Tarascon, J.-M.; Armand, M. Issues and Challenges Facing Rechargeable Lithium Batteries. *Nature* **2001**, *414*, 359−367.

(3) Pan, H.; Hu, Y.-S.; Chen, L. Room-Temperature Stationary Sodium-Ion Batteries for Large-Scale Electric Energy Storage. *Energy Environ. Sci.* **2013**, *6*, 2338−2360.

(4) Fang, Y.; Xiao, L.; Chen, Z.; Ai, X.; Cao, Y.; Yang, H. Recent Advances in Sodium-Ion Battery Materials. *Electrochem. Energ. Rev.* **2018**, *1*, 294−323.

(5) Wang, T.; Su, D.; Shanmukaraj, D.; Rojo, T.; Armand, M.; Wang, G. Electrode Materials for Sodium-Ion Batteries: Considerations on Crystal Structures and Sodium Storage Mechanisms. *Electrochem. Energ. Rev.* **2018**, *1*, 200−237.

(6) Slater, M. D.; Kim, D.; Lee, E.; Johnson, C. S. Sodium-Ion Batteries. *Adv. Funct. Mater.* **2013**, *23*, 947−958.

(7) Luo, W.; Shen, F.; Bommier, C.; Zhu, H.; Ji, X.; Hu, L. Na-Ion Battery Anodes: Materials and Electrochemistry. *Acc. Chem. Res.* **2016**, *49*, 231−240.

(8) Kang, H.; Liu, Y.; Cao, K.; Zhao, Y.; Jiao, L.; Wang, Y.; Yuan, H. Update on Anode Materials for Na-ion Batteries. *J. Mater. Chem. A* **2015**, *3*, 17899−17913.

(9) Xiao, W.; Sun, Q.; Liu, J.; Xiao, B.; Glans, P.-A.; Li, J.; Li, R.; Guo, J.; Yang, W.; Sham, T.-K.; Sun, X. Utilizing the Full Capacity of Carbon Black as Anode for Na-ion Batteries via Solvent Co-intercalation. *Nano Res.* **2017**, *10*, 4378−4387.

(10) Fu, Y.; Wei, Q.; Zhang, G.; Sun, S. Advanced Phosphorus-Based Materials for Lithium/Sodium-Ion Batteries: Recent Developments and Future Perspectives. *Adv. Energy Mater.* **2018**, *8*, 1703058.

(11) Zhang, Y.; Rui, X.; Tang, Y.; Liu, Y.; Wei, J.; Chen, S.; Leow, W. R.; Li, W.; Liu, Y.; Deng, J.; Ma, B.; Yan, Q.; Chen, X. Wet-Chemical Processing of Phosphorus Composite Nanosheets for High-Rate and High-Capacity Lithium-Ion Batteries. *Adv. Energy Mater.* **2016**, *6*, 1502409.

(12) Zhang, Y.; Wang, H.; Luo, Z.; Tan, H. T.; Li, B.; Sun, S.; Li, Z.; Zong, Y.; Xu, Z. J.; Yang, Y.; Khor, K. A.; Yan, Q. An Air-Stable Densely Packed Phosphorene-Graphene Composite Toward Advanced Lithium Storage Properties. *Adv. Energy Mater.* **2016**, *6*, 1600453.

(13) Sun, J.; Lee, H.-W.; Pasta, M.; Yuan, H.; Zheng, G.; Sun, Y.; Li, Y.; Cui, Y. A Phosphorene-Graphene Hybrid Material as a High-Capacity Anode for Sodium-Ion Batteries. *Nat. Nanotechnol.* **2015**, *10*, 980−985.

(14) Xu, G.-L.; Chen, Z.; Zhong, G.-M.; Liu, Y.; Yang, Y.; Ma, T.; Ren, Y.; Zuo, X.; Wu, X.-H.; Zhang, X.; Amine, K. Nanostructured Black Phosphorus/Ketjenblack-MWCNTs Composite as High Performance Anode Material for Sodium-ion Batteries. *Nano Lett.* **2016**, *16*, 3955−3965.

(15) Serrano-Ruiz, M.; Romerosa, A.; Lorenzo-Luis, P. Elemental Phosphorus and Electromagnetic Radiation. *Eur. J. Inorg. Chem.* **2014**, 1587−1598.

(16) Yabuuchi, N.; Kubota, K.; Dahbi, M.; Komaba, S. Research Development on Sodium-Ion Batteries. *Chem. Rev.* **2014**, *114*, 11636−11682.

(17) Extance, P.; Elliott, S. R. Pressure Dependence of the Electrical Conductivity of Amorphous Red Phosphorus. *Philos. Mag. B* **1981**, *43*, 469−483.

(18) Qian, J.; Wu, X.; Cao, Y.; Ai, X.; Yang, H. High Capacity and Rate Capability of Amorphous Phosphorus for Sodium Ion Batteries. *Angew. Chem., Int. Ed.* **2013**, *52*, 4633−4636.

(19) Kim, Y.; Park, Y.; Choi, A.; Choi, N.-S.; Kim, J.; Lee, J.; Ryu, J. H.; Oh, S. M.; Lee, K. T. An Amorphous Red Phosphorus/Carbon Composite as a Promising Anode Material for Sodium Ion Batteries. *Adv. Mater.* **2013**, *25*, 3045−3049.

(20) Li, W.-J.; Chou, S.-L.; Wang, J.-Z.; Liu, H.-K.; Dou, S.-X. Simply Mixed Commercial Red Phosphorus and Carbon Nanotube Composite with Exceptionally Reversible Sodium-Ion Storage. *Nano Lett.* **2013**, *13*, 5480−5484.

(21) Li, W.-J.; Chou, S.-L.; Wang, J.-Z.; Liu, H.-K.; Dou, S.-X. Significant Enhancement of the Cycling Performance and Rate Capability of the P/C Composite via Chemical Bonding (P−C). *J. Mater. Chem. A* **2015**, *4*, 505−511.

(22) Yu, Z.; Song, J.; Gordin, M. L.; Yi, R.; Tang, D.; Wang, D. Phosphorus-Graphene Nanosheet Hybrids as Lithium-Ion Anode with Exceptional High-Temperature Cycling Stability. *Adv. Sci.* **2015**, *2*, 1400020.

(23) Lee, G.-H.; Jo, M. R.; Zhang, K.; Kang, Y.-M. A Reduced Graphene Oxide-Encapsulated Phosphorus/Carbon Composite as a Promising Anode Material for High-Performance Sodium-Ion Batteries. *J. Mater. Chem. A* **2017**, *5*, 3683−3690.

(24) Sun, J.; Lee, H.-W.; Pasta, M.; Sun, Y.; Liu, W.; Li, Y.; Lee, H. R.; Liu, N.; Cui, Y. Carbothermic Reduction Synthesis of Red Phosphorus-Filled 3D Carbon Material as a High Capacity Anode for Sodium Ion Batteries. *Energy Storage Mater.* **2016**, *4*, 130−136.

(25) Qian, J.; Xiong, Y.; Cao, Y.; Ai, X.; Yang, H. Synergistic Na-Storage Reactions in Sn_4P_3 as a High-Capacity, Cycle-stable Anode of Na-Ion Batteries. *Nano Lett.* **2014**, *14*, 1865−1869.

(26) Fan, X.; Mao, J.; Zhu, Y.; Luo, C.; Suo, L.; Gao, T.; Han, F.; Liou, S.-C.; Wang, C. Superior Stable Self-Healing SnP_3 Anode for Sodium-Ion Batteries. *Adv. Energy Mater.* **2015**, *5*, 1500174.

(27) Lu, Y.; Zhou, P.; Lei, K.; Zhao, Q.; Tao, Z.; Chen, J. Selenium Phosphide (Se_4P_4) as a New and Promising Anode Material for Sodium-Ion Batteries. *Adv. Energy Mater.* **2017**, *7*, 1601973.

(28) Li, W.; Ke, L.; Wei, Y.; Guo, S.; Gan, L.; Li, H.; Zhai, T.; Zhou, H. Highly Reversible Sodium Storage in a GeP_5/C Composite Anode with Large Capacity and Low Voltage. *J. Mater. Chem. A* **2017**, *5*, 4413−4420.

(29) Li, W.-J.; Chou, S.-L.; Wang, J.-Z.; Liu, H.-K.; Dou, S.-X. A New, Cheap, and Productive FeP Anode Material for Sodium-Ion Batteries. *Chem. Commun.* **2015**, *51*, 3682−3685.

(30) Zhao, F.; Han, N.; Huang, W.; Li, J.; Ye, H.; Chen, F.; Li, Y. Nanostructured CuP_2/C Composites as High-Performance Anode Materials for Sodium Ion Batteries. *J. Mater. Chem. A* **2015**, *3*, 21754−21759.

(31) Wu, C.; Kopold, P.; van Aken, P. A.; Maier, J.; Yu, Y. High Performance Graphene/Ni_2P Hybrid Anodes for Lithium and Sodium Storage through 3D Yolk-Shell-Like Nanostructural Design. *Adv. Mater.* **2016**, *29*, 1604015.

(32) Kim, S.-O.; Manthiram, A. High-Performance Red P-Based P−TiP_2−C Nanocomposite Anode for Lithium-Ion and Sodium-Ion Storage. *Chem. Mater.* **2016**, *28*, 5935−5942.

(33) Wang, L.; He, X.; Li, J.; Sun, W.; Gao, J.; Guo, J.; Jiang, C. Nano-structured Phosphorus Composite as High-Capacity Anode Materials for Lithium Batteries. *Angew. Chem., Int. Ed.* **2012**, *51*, 9034−9037.

(34) Li, W.; Yang, Z.; Jiang, Y.; Yu, Z.; Gu, L.; Yu, Y. Crystalline Red Phosphorus Incorporated with Porous Carbon Nanofibers as Flexible Electrode for High Performance Lithium-Ion Batteries. *Carbon* **2014**, *78*, 455−462.

(35) Zhu, Y.; Wen, Y.; Fan, X.; Gao, T.; Han, F.; Luo, C.; Liou, S.-C.; Wang, C. Red Phosphorus−Single-Walled Carbon Nanotube Composite as a Superior Anode for Sodium Ion Batteries. *ACS Nano* **2015**, *9*, 3254−3264.

(36) Yuan, T.; Ruan, J.; Peng, C.; Sun, H.; Pang, Y.; Yang, J.; Ma, Z.-F.; Zheng, S. 3D Red Phosphorus/Sheared CNT Sponge for High

Performance Lithium-Ion Battery Anodes. *Energy Storage Mater.* **2018**, *13*, 267−273.

(37) Li, W.; Yang, Z.; Li, M.; Jiang, Y.; Wei, X.; Zhong, X.; Gu, L.; Yu, Y. Amorphous Red Phosphorus Embedded in Highly Ordered Mesoporous Carbon with Superior Lithium and Sodium Storage Capacity. *Nano Lett.* **2016**, *16*, 1546−1553.

(38) Li, W.; Hu, S.; Luo, X.; Li, Z.; Sun, X.; Li, M.; Liu, F.; Yu, Y. Confined Amorphous Red Phosphorus in MOF-Derived N-Doped Microporous Carbon as a Superior Anode for Sodium-Ion Battery. *Adv. Mater.* **2017**, *29*, 1605820.

(39) Zhang, C.; Wang, X.; Liang, Q.; Liu, X.; Weng, Q.; Liu, J.; Yang, Y.; Dai, Z.; Ding, K.; Bando, Y.; Tang, J.; Golberg, D. Amorphous Phosphorus/Nitrogen-Doped Graphene Paper for Ultra-stable Sodium-Ion Batteries. *Nano Lett.* **2016**, *16*, 2054−2060.

(40) Gao, H.; Zhou, T.; Zheng, Y.; Liu, Y.; Chen, J.; Liu, H.; Guo, Z. Integrated Carbon/Red Phosphorus/Graphene Aerogel 3D Architecture via Advanced Vapor-Redistribution for High-Energy Sodium-Ion Batteries. *Adv. Energy Mater.* **2016**, *6*, 1601037.

(41) Chang, W.-C.; Tseng, K.-W.; Tuan, H.-Y. Solution Synthesis of Iodine-Doped Red Phosphorus Nanoparticles for Lithium-Ion Battery Anodes. *Nano Lett.* **2017**, *17*, 1240−1247.

(42) Zhou, J.; Liu, X.; Cai, W.; Zhu, Y.; Liang, J.; Zhang, K.; Lan, Y.; Jiang, Z.; Wang, G.; Qian, Y. Wet-Chemical Synthesis of Hollow Red-Phosphorus Nanospheres with Porous Shells as Anodes for High-Performance Lithium-Ion and Sodium-Ion Batteries. *Adv. Mater.* **2017**, *29*, 1700214.

(43) Island, J. O.; Steele, G. A.; Zant, H. S. J. v. d.; Castellanos-Gomez, A. Environmental Instability of Few-layer Black Phosphorus. *2D Mater* **2015**, *2*, 011002.

(44) Li, Y.; Hu, Y.-S.; Li, H.; Chen, L.; Huang, X. A Superior Low-Cost Amorphous Carbon Anode Made from Pitch and Lignin for Sodium-Ion Batteries. *J. Mater. Chem. A* **2015**, *4*, 96−104.

(45) Yuan, D.; Cheng, J.; Qu, G.; Li, X.; Ni, W.; Wang, B.; Liu, H. Amorphous Red Phosphorous Embedded in Carbon Nanotubes Scaffold as Promising Anode Materials for Lithium-Ion Batteries. *J. Power Sources* **2016**, *301*, 131−137.

(46) Song, J.; Yu, Z.; Gordin, M. L.; Hu, S.; Yi, R.; Tang, D.; Walter, T.; Regula, M.; Choi, D.; Li, X.; Manivannan, A.; Wang, D. Chemically Bonded Phosphorus/Graphene Hybrid as a High Performance Anode for Sodium-Ion Batteries. *Nano Lett.* **2014**, *14*, 6329−6335.

(47) Fuge, G. M.; May, P. W.; Rosser, K. N.; Pearce, S. R. J.; Ashfold, M. N. R. Laser Raman and X-ray Photoelectron Spectroscopy of Phosphorus Containing Diamond-Like Carbon Films Grown by Pulsed Laser Ablation Methods. *Diamond Relat. Mater.* **2004**, *13*, 1442−1448.

(48) Nicotra, G.; Politano, A.; Mio, A. M.; Deretzis, I.; Hu, J.; Mao, Z. Q.; Wei, J.; La Magna, A.; Spinella, C. Absorption Edges of Black Phosphorus: A Comparative Analysis. *Phys. Status Solidi B* **2016**, *253*, 2509−2514.

(49) Engemann, C.; Franke, R.; Hormes, J.; Lauterbach, C.; Hartmann, E.; Clade, J.; Jansen, M. X-ray Absorption Near-Edge Spectroscopy (XANES) at the Phosphorus K-Edge of Triorgano-phosphinechalcogenides. *Chem. Phys.* **1999**, *243*, 61−75.

(50) Morel, F. L.; Pin, S.; Huthwelker, T.; Ranocchiari, M.; van Bokhoven, J. A. Phosphine and Phosphine Oxide Groups in Metal-Organic Frameworks Detected by P K-Edge XAS. *Phys. Chem. Chem. Phys.* **2015**, *17*, 3326−3331.

(51) Ingall, E. D.; Brandes, J. A.; Diaz, J. M.; de Jonge, M. D.; Paterson, D.; McNulty, I.; Elliott, W. C.; Northrup, P. Phosphorus K-edge XANES Spectroscopy of Mineral Standards. *J. Synchrotron Radiat.* **2011**, *18*, 189−197.

(52) Tian, W.; Wang, L.; Huo, K.; He, X. Red Phosphorus Filled Biomass Carbon as High-capacity and Long-life Anode for Sodium-Ion Batteries. *J. Power Sources* **2019**, *430*, 60−66.

(53) Kim, Y.; Kim, Y.; Choi, A.; Woo, S.; Mok, D.; Choi, N.-S.; Jung, Y. S.; Ryu, J. H.; Oh, S. M.; Lee, K. T. Tin Phosphide as a Promising Anode Material for Na-Ion Batteries. *Adv. Mater.* **2014**, *26*, 4139−4144.

(54) Xu, K. Electrolytes and Interphases in Li-Ion Batteries and Beyond. *Chem. Rev.* **2014**, *114*, 11503−11618.

(55) Wan, S.; Tieu, A. K.; Zhu, Q.; Zhu, H.; Cui, S.; Mitchell, D. R.; Kong, C.; Cowie, B.; Denman, J. A.; Liu, R. Chemical Nature of Alkaline Polyphosphate Boundary Film at Heated Rubbing Surfaces. *Sci. Rep.* **2016**, *6*, 26008.

(56) Yin, Z.; Kasrai, M.; Bancroft, G. M.; Tan, K. H.; Feng, X. X-ray-Absorption Spectroscopic Studies of Sodium Polyphosphate Glasses. *Phys. Rev. B: Condens. Matter Mater. Phys.* **1995**, *51*, 742−750.

(57) Yabuuchi, N.; Matsuura, Y.; Ishikawa, T.; Kuze, S.; Son, J.-Y.; Cui, Y.-T.; Oji, H.; Komaba, S. Phosphorus Electrodes in Sodium Cells: Small Volume Expansion by Sodiation and the Surface-Stabilization Mechanism in Aprotic Solvent. *ChemElectroChem* **2014**, *1*, 580−589.

(58) Song, J.; Yu, Z.; Gordin, M. L.; Li, X.; Peng, H.; Wang, D. Advanced Sodium Ion Battery Anode Constructed via Chemical Bonding between Phosphorus, Carbon Nanotube, and Cross-Linked Polymer Binder. *ACS Nano* **2015**, *9*, 11933−11941.

(59) Liu, S.; Feng, J.; Bian, X.; Liu, J.; Xu, H.; An, Y. A Controlled Red Phosphorus@Ni−P Core@Shell Nanostructure as an Ultralong Cycle-Life and Superior High-Rate Anode for Sodium-Ion Batteries. *Energy Environ. Sci.* **2017**, *10*, 1222−1233.

(60) Yang, S.; Wang, D.; Liang, G.; Yiu, Y. M.; Wang, J.; Liu, L.; Sun, X.; Sham, T.-K. Soft X-ray XANES Studies of Various Phases Related to LiFePO₄ Based Cathode Materials. *Energy Environ. Sci.* **2012**, *5*, 7007.

(61) Kruse, J.; Leinweber, P.; Eckhardt, K.-U.; Godlinski, F.; Hu, Y.; Zuin, L. Phosphorus L2,3-Edge XANES: Overview of Reference Compounds. *J. Synchrotron Radiat.* **2009**, *16*, 247−259.

(62) Ferrett, T. A.; Piancastelli, M. N.; Lindle, D. W.; Heimann, P. A.; Shirley, D. A. Si 2p and 2s Resonant Excitation and Photoionization in SiF₄. *Phys. Rev. A: At., Mol., Opt. Phys.* **1988**, *38*, 701−710.

(63) Harp, G. R.; Han, Z. L.; Tonner, B. P. X-ray Absorption Near Edge Structures of Intermediate Oxidation States of Silicon in Silicon Oxides during Thermal Desorption. *J. Vac. Sci. Technol., A* **1990**, *8*, 2566−2569.

(64) Hansen, P. L.; Brydson, R.; McComb, D. W. p → p-Like Transitions at the Silicon L2,3-edges of Silicates. *Microsc., Microanal., Microstruct.* **1992**, *3*, 213−219.

(65) Huang, Y.; Qiao, J.; He, K.; Bliznakov, S.; Sutter, E.; Chen, X.; Luo, D.; Meng, F.; Su, D.; Decker, J.; Ji, W.; Ruoff, R. S.; Sutter, P. Interaction of Black Phosphorus with Oxygen and Water. *Chem. Mater.* **2016**, *28*, 8330−8339.

(66) Meng, X.; Yang, X.-Q.; Sun, X. Emerging Applications of AtomicLayer Deposition for Lithium-Ion Battery Studies. *Adv. Mater.* **2012**, *24*, 3589−3615.

(67) Li, X.; Lushington, A.; Sun, Q.; Xiao, W.; Liu, J.; Wang, B.; Ye, Y.; Nie, K.; Hu, Y.; Xiao, Q.; Li, R.; Guo, J.; Sham, T.-K.; Sun, X. Safe and Durable High-Temperature Lithium-Sulfur Batteries via Molecular Layer Deposited Coating. *Nano Lett.* **2016**, *16*, 3545−3549.

(68) Li, X.; Lushington, A.; Liu, J.; Li, R.; Sun, X. Superior Stable Sulfur Cathodes of Li-S Batteries Enabled by Molecular Layer Deposition. *Chem. Commun.* **2014**, *50*, 9757−9760.

(69) Zhao, Y.; Sun, X. Molecular Layer Deposition Technique for Energy Conversion and Storage. *ACS Energy Lett.* **2018**, *3*, 899−914.

(70) Zhao, Y.; Goncharova, L. V.; Lushington, A.; Sun, Q.; Yadegari, H.; Wang, B.; Xiao, W.; Li, R.; Sun, X. Superior Stable and Long Life Sodium Metal Anodes Achieved by Atomic Layer Deposition. *Adv. Mater.* **2017**, *29*, 1606663.